CHEMISTRY OF MATERIALS

pubs.acs.org/cm

Article

Decoding the Mechanisms of Room-Temperature Solid-State Synthesis of Halide Perovskites

Mahsa Shekarnoush, Leunam Fernandez-Izquierdo, Francisco S. Aguirre-Tostado, Zeshaan H. Shamsi, and Manuel A. Quevedo-Lopez*

Cite This: *Chem. Mater.* 2023, 35, 8909−8921

Read Online

ACCESS | Metrics & More | Article Recommendations | Supporting Information

ABSTRACT: Room-temperature solid-state synthesis of halide perovskites is a simple, single-step, efficient, and cost-effective method to synthesize halide perovskite precursors that can be subsequently used to deposit thin films by using various techniques. Solid-state methods also reduce and, in some cases, eliminate additional time-consuming treatments and purification steps. Therefore, understanding the reaction mechanism is crucial to the controlled synthesis of various perovskite systems. This study explores the reaction mechanisms and associated kinetics of room-temperature solid-state halide perovskites synthesized by using a planetary ball-milling system. A $CsPbBr_3$ system (ABX_3) is used as a reference to study the exchange of A, B, and X sites with methylammonium (MA^+), Cd^{2+}, and Cl^-, respectively. Various characterization techniques, including X-ray diffraction (XRD), X-ray photoelectron spectroscopy (XPS), ultraviolet−visible (UV−vis) spectroscopy, and field emission scanning electron microscopy (FESEM), are used to analyze the resulting materials at different reaction times. The findings highlight the significance of factors such as perovskite formation energy, the particle size distribution of precursors, bond dissociation energy, molecular weight of the A cation, and the size and mobility of the X^- ion in influencing the mechanism and kinetics of the reactions. Furthermore, the conversion of precursors to perovskites is investigated using XPS, which provides valuable information on the chemical shifts of the precursors and perovskite materials and can serve as a reliable source for future studies.

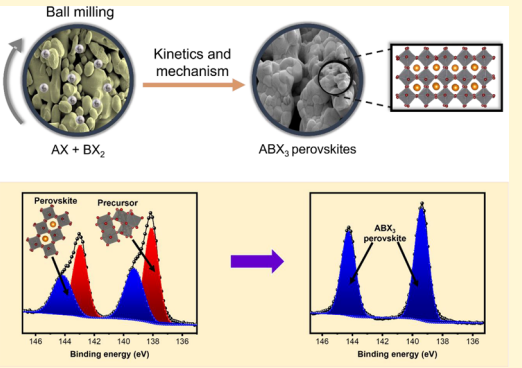

Downloaded via UNIV OF TEXAS AT DALLAS on January 27, 2025 at 12:29:26 (UTC).
See https://pubs.acs.org/sharingguidelines for options on how to legitimately share published articles.

INTRODUCTION

Halide perovskite materials have the analogous crystalline structure of the mineral calcium titanate ($CaTiO_3$) and the general formula ABX_3.[1] In halide perovskites, the "A" site can be occupied by alkali metals such as K^+, Rb^+, Cs^+,[2−4] or organic cations such as methylammonium (MA^+) or formamidinium (FA^+).[5,6] In contrast, the "B" site is occupied by alkaline or transition metal cations (Mg^{2+}, Ca^{2+}, Cd^{2+}, and Ni^{2+})[7−10] or divalent cations from group IV of the periodic table, such as Pb^{2+} and Sn^{2+}.[5,11−13] Lastly, the "X" site is typically occupied by halogen ions (Cl^-, Br^-, and I^-).[14] Several criteria must be fulfilled for materials with the ABX_3 formula to form a perovskite crystalline structure. First, the overall charge of the cations and anions must be electronically neutral or zero.[15] Second, the $\mu = R_B/R_X$ must be between $0.44 \leq \mu \leq 0.9$.[16] This octahedral factor range enables the appropriate geometric arrangement that results in a structurally stable perovskite crystal lattice. Lastly, the Goldschmidt tolerance factor (t),[17] given by $t = (R_A + R_X)/\sqrt{2}(R_B + R_X)$, should be $0.8 \leq t \leq 1$, where R_A, R_B, and R_X represent the ionic radii of A, B, and X sites, respectively.[16,18]

Halide perovskites have gained significant interest in recent years for a diverse range of applications, including solar cells,[19] photo rechargeable batteries,[20] light emission diode (LED) devices, lasers,[21] and X-ray detectors[22] due to their high atomic number (Z) and absorption coefficient.[23,24] Additionally, halide perovskites offer the unique ability to dynamically adjust their band gap, which is crucial for semiconductor applications.[25,26] Furthermore, halide perovskite materials exhibit high charge carrier mobilities (1−100 $cm^2/(V\ s)$),[27] considerable diffusion lengths (>10 μm),[28] and relatively short charge-relaxation times spanning from tens to hundreds of picoseconds.[29] These unique characteristics position halide perovskites as promising materials for advanced optoelectronic devices.[18,30]

Numerous reports suggest that the synthesis method plays a crucial role in the properties of the halide perovskites and can impact their composition, morphology, purity, and stability.[31−35] Solution-based methods have been widely used to

Received: June 9, 2023
Revised: September 29, 2023
Published: October 19, 2023

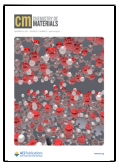

ACS Publications

© 2023 American Chemical Society

prepare various halide perovskites and typically involve precursor solutions at elevated temperatures, stabilizing agents or surfactants, postsynthesis treatments, and subsequent purification steps.[36−39] Solution-based methods have some unresolved issues, such as partial solubility of specific precursors in standard solvents, limited solution stability, low yield, and complex purification procedures.[40−43] To overcome these challenges, solid-state methods have emerged as a promising alternative for synthesizing halide perovskites. Solid-state methods offer advantages such as simplified synthesis processes, enhanced long-term stability, and potentially higher yields. They are promising routes to address the limitations associated with solution-based approaches and achieve better composition control, favorable morphology, and purity of halide perovskite materials.[36]

Several solid-state methods have been used for the synthesis of halide perovskites, including thermal annealing,[44] melt-solidification,[45] and mechanochemical methods.[46−49] Among these techniques, mechanochemical methods have gained particular attention for the synthesis of polycrystalline halide perovskites. Mechanochemical methods offer several advantages, including room temperature synthesis, reduced synthesis steps, improved stoichiometric control, elimination of complex purification steps, and compatibility with a wide range of halide perovskite compositions.[46,50−52] One of the most promising mechanochemical methods is ball milling. Ball milling involves the dynamic grinding of precursors using suitable balls in a reaction vessel.[53] The balls utilized in the ball-milling system play a crucial role as they interact with the precursors, facilitating the reduction of powders to smaller particles and supplying the necessary energy for precursor reactions.[46,48] In a planetary ball milling system, high energy is acquired by rapidly rotating the jar and disk, which generates a strong centrifugal force on the milling balls.[54] The impact energy can be controlled by adjusting the rotation speed and direction to achieve the desired outcome.

Numerous research reports have highlighted the successful use of ball-milling techniques for synthesizing a diverse range of halide perovskites. These compositions span $CsPbBr_3$,[55] $MAPbBr_3$,[56] $MAPbI_3$,[57] $CsSnBr_3$,[52] (MA, FA)PbI_3,[58] and $CsPbCl_3$,[59] and more, with the intention of exploring various applications.

Despite advancements in the ball-milling synthesis of halide perovskites, a significant gap persists in comprehending the underlying kinetics and mechanisms.[55,60] This gap is particularly crucial when considering the potential of this technique in synthesizing a diverse array of perovskites. To fully utilize this synthesis method and surpass the limitations of solution-based approaches, a thorough understanding of the effective factors in the kinetics and mechanism of these reactions is essential. Gaining insights into these factors enables researchers to optimize the synthesis process, enhance material quality, and expand the potential applications of halide perovskites.

In this work, we aimed to study the kinetics and mechanism of the solid-state synthesis of halide perovskites. To accomplish this, we optimized the ball-milling synthesis parameters to produce large (gram) scale of $CsPbBr_3$, $MAPbBr_3$, $CsCdBr_3$, and $CsPbCl_3$ compounds, demonstrating exceptional humidity and air stability. Through the successful synthesis of these target compounds, we delved into the influence of A, B, and X sites during the room-temperature solid-state synthesis of halide perovskites. The investigation into the reaction mechanism and kinetics for different perovskite compositions was carried out using different characterization techniques, including XRD, XPS, UV−vis, PL, and FESEM. XRD analysis enabled the identification of impurities and byproducts, while XPS provided insights into the binding energy of elements within the precursors and the resulting perovskite systems. FESEM imaging was employed to analyze the size and morphology of the precursor materials and products. Our study utilized XPS to carefully follow the kinetics of precursor-to-perovskite conversion and correlated these findings with XRD analysis. Additionally, the chemical shifts identified by XPS can be used as reliable sources for assessing the purity of the perovskite materials. Based on the data collected and analyzed, we proposed a plausible mechanism for the synthesis method under investigation. Our study suggests that the precursors' decomposition, the B−X bond energy in the $[BX_3]^-$ octahedral framework, the diffusion rate of A cation, and the formation energy of the desired perovskites all play critical roles in the kinetics and mechanism of solid-state synthesis of halide perovskites.

EXPERIMENTAL SECTION

Materials. Cesium bromide (CsBr, ultradry, 99.9%) and cadmium bromide ($CdBr_2$, anhydrous, 98%) were acquired from Alfa-Aesar. Lead(II) bromide ($PbBr_2$, 99.999%), lead(II) chloride ($PbCl_2$, 99.999%), cesium chloride (CsCl, 99.999%), and methylammonium bromide (MABr) were acquired from Sigma-Aldrich. The stainless-steel balls (2 mm), stainless-steel milling jars, and the high Energy Vertical Planetary Ball Mill were acquired from MSE Supplies LLC.

ABX_3 Synthesis. For each reaction, 2.5 mmol of AX (either CsBr, CsCl, or MABr) and 2.5 mmol of BX_2 (either $PbBr_2$, $PbCl_2$, or $CdBr_2$) and 5 g of stainless-steel balls with a diameter of 2 mm per gram of precursors were first added to the jars. The jars were then placed in a vertical planetary ball-milling system. Pre-eliminate results suggested that the order in which the precursors and balls are added to the jar plays an essential role in the resulting material and indicated that more pure products are obtained when the precursors are added before the balls. This process was followed for all experiments described in this study and the solid-state reaction time varied from 0 to 12 h at a constant rotational velocity of 700 rpm. Samples were collected at several time intervals and characterized using various methods. The materials were weighed accurately and introduced into the ball milling jar under atmospheric ambient conditions. Samples labeled as $t = 0$ h were prepared by gently mixing the precursors in air at room temperature to ensure a homogeneous distribution of the materials.

Material Characterization. The crystalline structure of the samples was studied by powder X-ray diffraction (XRD) methods in the Bragg−Brentano[61] geometry with a theta/2-theta goniometer. The XRD analyses were carried out in a Rigaku SmartLab X-ray diffraction system equipped with a copper CuKα radiation source (λ = 1.5406 Å) and obtained using a current of 30 mA at a voltage of 40 kV and a scan speed of 3 deg/min. X-ray photoelectron spectroscopy (XPS) was used to conduct the chemical analysis in a PHI 5600 system with a monochromatic Al Ka X-ray source ($h\nu$ = 1486.7 eV). The XPS spectra were recorded with a pass energy of 29.35 eV and a step size of 0.125 eV. The X-ray incidence angle relative to the sample surface was 45 deg. The spectra were recorded under ultrahigh vacuum conditions (~10^{-9} mbar) for 45 min in the dark. UV−vis measurements were performed using an Agilent UV−vis-NIR system equipped with a Mercury arc lamp and multiangle reflection (R) capability. The photoluminescence (PL) was recorded utilizing the Ocean Optics QE65000 spectrometer, with an excitation source of a 405 nm constant-wave laser and a 450 nm long-pass filter. Finally, a field emission scanning electron microscopy (FESEM) Zeiss Supra40 device was used for the morphological and size analysis of the powders. The analysis of the area distribution from SEM images for

https://doi.org/10.1021/acs.chemmater.3c01440
Chem. Mater. 2023, 35, 8909−8921

Table 1. Calculated Tolerance and Octahedral Factors for $CsPbBr_3$, $MAPbBr_3$, $CsCdBr_3$, and $CsPbCl_3$ Compositions

composition	R_A (pm)	R_B (pm)	R_X (pm)	tolerance factor t	octahedral factor μ
$CsPbBr_3$	Cs^+ (188)	Pb^{2+} (119)	Br^- (196)	0.862	0.607
$MAPbBr_3$	MA^+ (180)[69]	Pb^{2+} (119)	Br^- (196)	0.844	0.607
$CsCdBr_3$	Cs^+ (188)	Cd^{2+} (95)	Br^- (196)	0.933	0.484
$CsPbCl_3$	Cs^+ (188)	Pb^{2+} (119)	Cl^- (181)	0.870	0.657

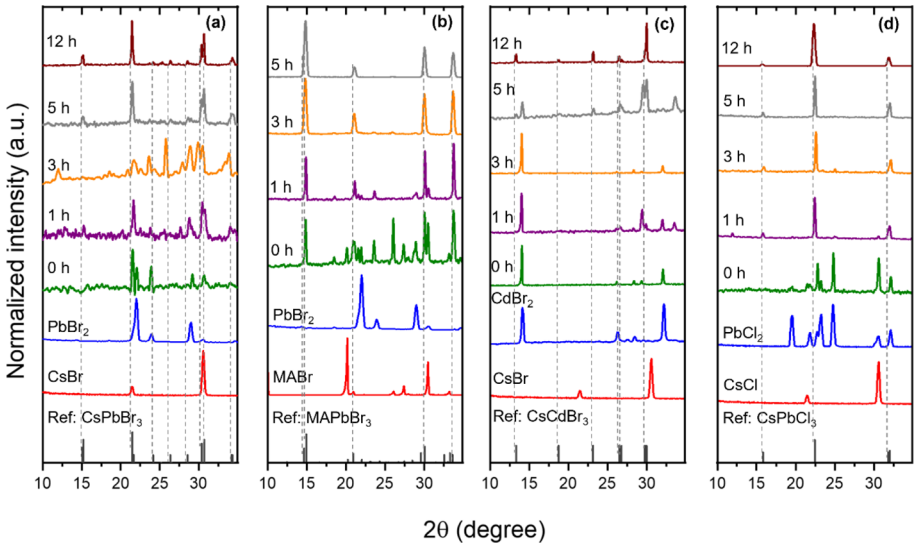

Figure 1. XRD patterns of ball-milled $CsPbBr_3$ (a), $MAPbBr_3$ (b), $CsCdBr_3$, (c), and $CsPbCl_3$ (d) for different milling times.

precursors and perovskites was performed using ImageJ software. VESTA Ver.3.5.8 software[62] is employed to visualize the crystalline structure of the precursors and perovskites.

RESULTS AND DISCUSSION

This article has two objectives. The first objective is to investigate the effects of replacing the A, B, and X sites in the ABX_3 formula during the ball-milling synthesis of halide perovskites. The second objective is to identify the associated reaction mechanism. These objectives are accomplished by carefully analyzing the evolution of the crystalline structure, chemical composition, and morphology of the synthesized perovskite materials. Four perovskite compositions were synthesized to accomplish these objectives. Comparing $CsPbBr_3$ (CPB) with $MAPbBr_3$ (MPB) provides insights into the role of site A while comparing CPB with $CsCdBr_3$ (CCB) helps understand the role of site B. Similarly, comparing CPB with $CsPbCl_3$ (CPC) provides information about site X. The following sections show the results of each of these comparisons, aiming to elucidate the impact of A, B, and X on the evolution of chemical and structural properties of ABX_3 as a function of milling conditions.

Table 1 shows the tolerance and octahedral factors for the selected perovskite compositions. These values were calculated using the Shannon effective ionic radii,[63] which are compatible with the accepted theoretical ranges for halide perovskites. The tolerance factors for $CsPbBr_3$, $MAPbBr_3$, and $CsPbCl_3$ are all below 0.9, confirming their orthorhombic structure. In contrast, the tolerance factor for $CsCdBr_3$ is 0.933, suggesting its potential to adopt a cubic structure. This suggestion, which supports the likelihood of $CsCdBr_3$ adopting a cubic structure is also supported by a few references.[64−66] However, it is noteworthy that most studies agree on $CsCdBr_3$ adopting the hexagonal structure at room temperature.[67,68]

Role of A-Site Components Cs and MA in the (A)$PbBr_3$ System. The ABX_3 crystalline structure of halide perovskites consists of B (II) atoms surrounded by six halogen ions (X^-), forming $[BX_6]^{4-}$ octahedral units. These octahedra can arrange through corner-sharing, face-sharing, or edge-sharing in the $[BX_3]^-$ octahedron framework. To maintain charge balance, the "A" cations occupy cavities within the $[BX_3]^-$ octahedron network.[1] The ideal crystalline structure of perovskite materials is cubic; however, distortion of these $[BX_6]^{4-}$ octahedra leads to lower symmetry phases, such as the orthorhombic structure.[70,71] Within the perovskite family, various structural arrangements have evolved beyond the cubic structure. These structural variations are defined by the ABX_3 formula and are closely associated with the cubic framework. For instance, the hexagonal perovskite structure, as exemplified by the $BaNiO_3$ chain structure, features one-dimensional structures formed by the face-sharing of $[BX_6]^{4-}$ octahedral units.[72]

Figure 1a shows the XRD patterns of ball-milled $CsPbBr_3$ precursors as a function of time (t). The XRD patterns for t = 0 h show only the presence of the CsBr and $PbBr_2$ precursors. For samples processed for t = 1 h, two additional peaks, at 12.78° and 15.1°, are detected. The peak at 12.78° corresponds to the (012) plane of the trigonal phase of Cs_4PbBr_6,[73] as shown in Figure S1. The peak at 15.1° corresponds to the (100) plane for the orthorhombic $CsPbBr_3$ perovskite structure. For t = 3 h, in addition to the precursors and $CsPbBr_3$ perovskite peaks, an additional peak appears at 11.85°. This peak indicates the presence of the (002) plane of the tetragonal phase corresponding to $CsPb_2Br_5$[74] (see Figure S1). The presence of the precursors for short reaction times (1 and 3 h) is expected. However, the unexpected presence of the Cs_4PbBr_6, and $CsPb_2Br_5$ phases can be attributed to a nonuniform distribution of CsBr and $PbBr_2$ precursors at the

https://doi.org/10.1021/acs.chemmater.3c01440
Chem. Mater. 2023, 35, 8909−8921

early reaction stages. This inhomogeneity leads to variations in the molar ratio from the nominal 1:1 ($CsBr:PbBr_2$), resulting in the formation of these undesired phases. The large inhomogeneity of precursors at the beginning leads to the formation of CsBr and $PbBr_2$-rich regions that promote favorable conditions for the formation of Cs_4PbBr_6, and $CsPb_2Br_5$ phases. As a result, for reaction times shorter than 3 h, the large degree of inhomogeneity in the ball milling results in the presence of byproducts alongside the $CsPbBr_3$ perovskite phase. With a milling time of 5 h, the XRD pattern of $CsPbBr_3$ precursors shows the presence of a more prominent (100) plane corresponding to the orthorhombic perovskite structure of $CsPbBr_3$. This implies that extending the reaction time facilitates improved mixing of the precursors, resulting in a greater propensity for the formation of $CsPbBr_3$. Finally, the XRD analysis demonstrates that all the precursors completely convert into $CsPbBr_3$ perovskites within 12 h. The convergence of secondary phases into $CsPbBr_3$ is achieved due to the initial precursor ratio of 1:1 ($CsBr:PbBr_2$) in a ball-milling jar.

Figure 2 shows the ternary phase diagram for the Cs, Pb, and Br mixture under constant temperature and pressure

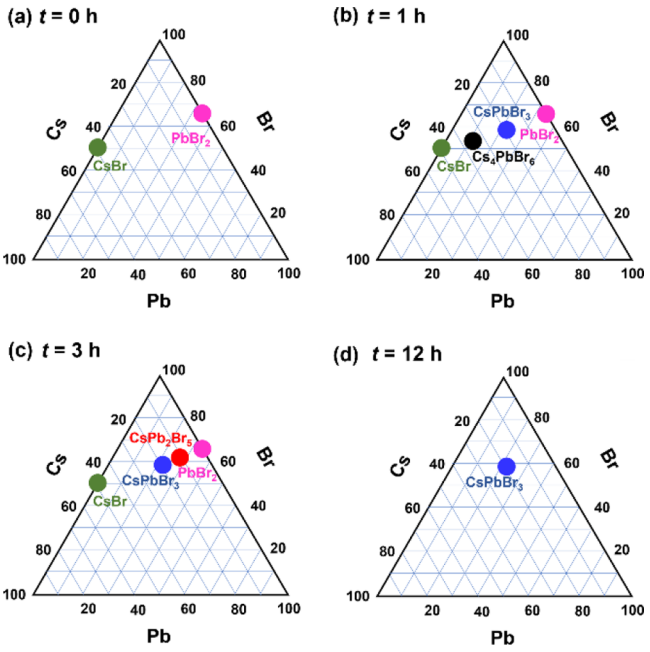

Figure 2. Ternary phase diagram for the mixture of Cs, Pb, and Br at 0 h (a), 1 h (b), 3 h (c), and 12 h (d). The black, blue, red, green, and purple symbols correspond to Cs_4PbBr_6, $CsPbBr_3$ and $CsPb_2Br_5$, CsBr, and $PbBr_2$.

conditions. The phase diagram shows the presence of CsBr and $PbBr_2$ precursors at 0 h (see Figure 2a). After 1 h, Cs-rich (Cs_4PbBr_6) and $CsPbBr_3$ phases appear in addition to the precursors (see Figure 2b). Subsequently, at t = 3 h, the Cs-rich phase disappears and a Pb-rich phase ($CsPb_2Br_5$) appears alongside $CsPbBr_3$ and the precursors (see Figure 2c). At t = 12 h, only the $CsPbBr_3$ phase is present (see Figure 2d). The results obtained from the XRD analysis are further supported by the chemical analysis shown in the XPS section.

Next, the impact of MA as an A-site component is analyzed. Figure 1 shows the XRD patterns of $MAPbBr_3$ as a function of ball milling time. Initially, at t = 0 h, only the diffraction peaks corresponding to the precursor materials would be expected. However, the presence of the peak at 15.1°, corresponding to the (100) plane of the orthorhombic phase of $MAPbBr_3$, provides evidence that a reaction has occurred between the precursor materials (MABr and $PbBr_2$) even after manual mixing. Moreover, diffraction peaks corresponding to MABr and $PbBr_2$ precursors are also observed for 0, 1, and 3 h of reaction time. The complete conversion of precursor materials into a pure $MAPbBr_3$ perovskite structure is achieved after 5 h, which is significantly faster compared to that of $CsPbBr_3$ (t = 12 h). Based on the results obtained from the A-site behavior, we can conclude that the kinetics of formation of the $APbBr_3$ perovskite structure depend on the concentration of available A cations. This availability is influenced by two key factors. The first factor involves the decomposition of the A-Br precursor. When comparing the decomposition of the A-Br bond, MA ($CH_3NH_3^+$) cations are more readily available than Cs^+ due to the lower bond energy in MA-Br (CH_3NH_3Br) compared with the bond energy between Cs and Br in Cs−Br. The second factor involves the diffusion of the A cation into the cavities of the $[PbBr_3]^-$ framework. Due to the lower molecular weight of MA^+ compared to Cs^+, MA^+ diffusion is more favored compared to Cs^+.[75] These two factors result in faster reaction kinetics and a substantially shorter conversion time for $MAPbBr_3$ compared to $CsPbBr_3$ during the room-temperature solid-state synthesis of halide perovskites.

Figure 3a shows the XPS regions for Cs $3d_{5/2}$, Pb 4f, and Br 3d for $CsPbBr_3$ and Figure 3b shows the N 1s, Pb 4f, and Br 3d for $MAPbBr_3$ at various milling times. These regions are used to obtain the elemental composition for each milling time. Furthermore, each peak is deconvoluted to distinguish the contribution of elements in the precursor from those in the formed perovskite (product). This is achievable by using the chemical shift, i.e., a change in the orbital binding energy associated with the bonding environment in each compound. Through this approach, it becomes possible to determine unreacted precursors at different milling times and simultaneously calculate the amount of perovskite formed.

The Cs $3d_{5/2}$ region has two chemical components, one at 725.8 eV that corresponds to Cs in the CsBr precursor (Cs_{CsBr} peak) and the other at 724.25 eV that corresponds to the Cs in the $CsPbBr_3$ perovskites (Cs_{CPB} peak).[76,77] To investigate the evolution of MA in the $MAPbBr_3$ system, the N 1s XPS region is used to estimate the concentration of MA as a function of the milling time. The XPS analysis of the N 1s region shows two distinct peaks, one at 402.80 eV which is assigned to N atoms in the CH_3NH_3Br precursor (N_{MABr} peak) and the other at 401.58 eV that corresponds to N atoms in the $MAPbBr_3$ perovskite (N_{MPB} peak).[78] The Pb 4f regions at the beginning of the reaction for both $CsPbBr_3$ and $MAPbBr_3$ show a peak at 141.96 eV corresponding to Pb $4f_{7/2}$. This peak is attributed to the presence of Pb atoms in the $PbBr_2$ precursors. Upon formation of the perovskite, an additional peak emerges at 143.27 eV (Pb $4f_{7/2}$), which is attributed to the Pb atoms in the $CsPbBr_3$ and $MAPbBr_3$ perovskites[77,79] (see Figure 3).

The Br 3d has two chemical components, one centered at 68.8 eV that is attributed to Br in the precursors of $MAPbBr_3$ (MABr and $PbBr_2$) and $CsPbBr_3$ (CsBr and $PbBr_2$). The second one at 68.45 eV is associated with the presence of Br in the $MAPbBr_3$ and $CsPbBr_3$ perovskite structures.[76] The peak areas obtained from the deconvoluted peaks in Figure 3 were used to determine the elemental composition for the different orbitals and milling times.[80]

https://doi.org/10.1021/acs.chemmater.3c01440
Chem. Mater. 2023, 35, 8909−8921

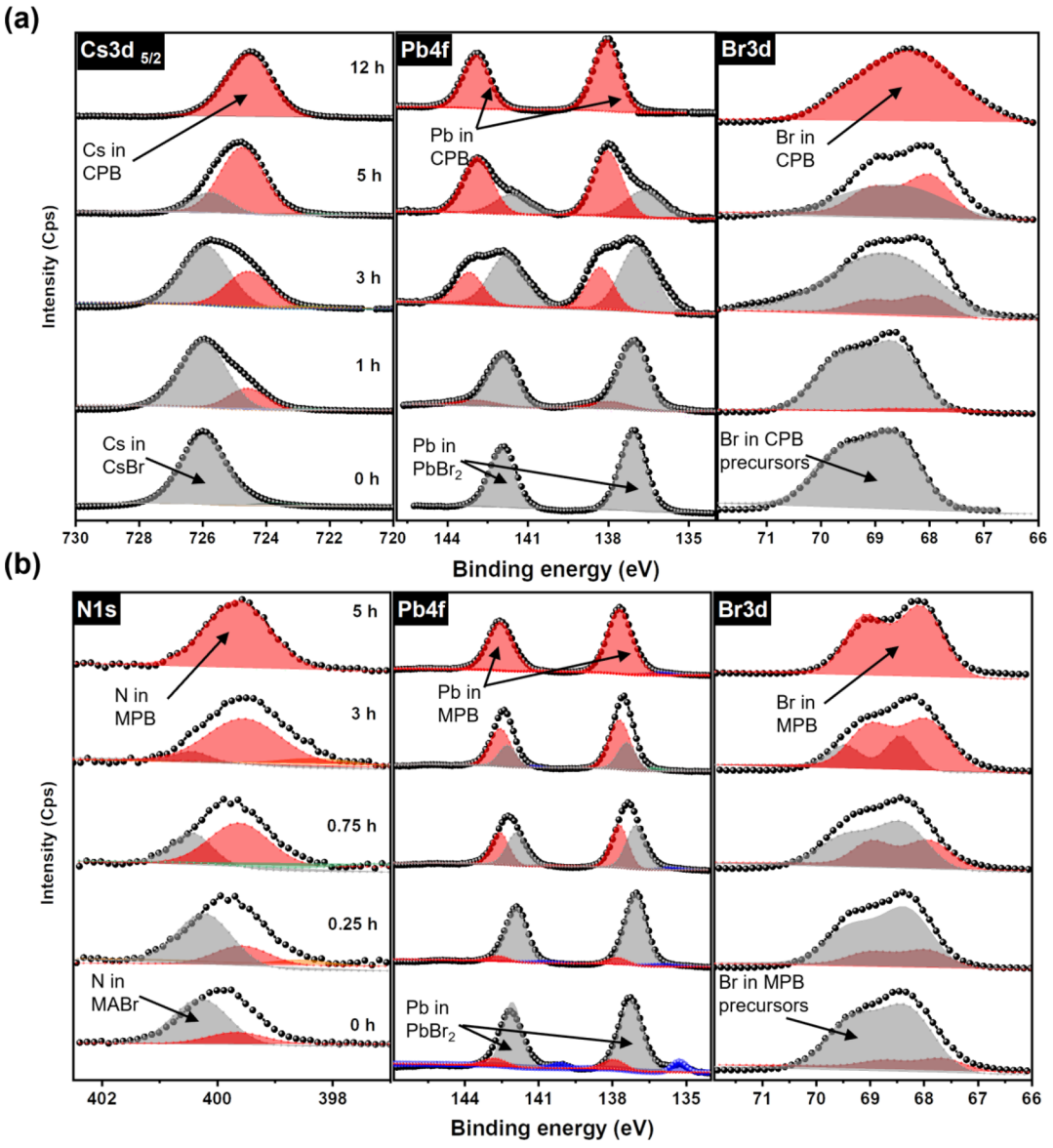

Figure 3. XPS results of ball-milled $CsPbBr_3$ (a) and $MAPbBr_3$ (b) precursors for different times. The red peaks correspond to the perovskites, and the gray peaks correspond to the precursors.

The compositional analysis for the two A-sites (Cs and MA) is shown in Figure 4. The evolution of unreacted precursors and the formed perovskite was determined by analyzing the atomic composition of Cs, Pb, and Br for $CsPbBr_3$ and N, Pb, and Br for $MAPbBr_3$. Regardless of the element used to determine the precursor/product composition in the reaction as a function of the milling time, the evolution behavior is the same.

The compositional analyses reveal distinct trends in the conversion and kinetics of formation between $MAPbBr_3$ and $CsPbBr_3$. Specifically, the N, Pb, and Br regions in $MAPbBr_3$ demonstrate faster precursor conversion to perovskites (t = 0 h) compared to $CsPbBr_3$ samples (t = 1 h). Consequently, pure $MAPbBr_3$ perovskites are achieved faster (t = 5 h), while the formation of pure $CsPbBr_3$ perovskites occurs at a longer time (t = 12 h).

The observed differences in conversion rates between $MAPbBr_3$ and $CsPbBr_3$ precursors highlight the role of distinct A-site cations in the perovskite formation process. The presence of weaker bonds in the MABr precursor materials, coupled with the lower molecular mass of MA cations, facilitates faster reaction kinetics in the direction of the $MAPbBr_3$ perovskite formation.

Role of B-Site Components Pb and Cd in the $Cs(B)Br_3$ System. The XRD patterns for the ball-milled synthesis of $CsCdBr_3$ as a function of time are shown in Figure 1c. No intermediate or perovskite phases are formed during the first 3 h. Only the characteristic peaks of the CsBr and $CdBr_2$ precursors are detected. However, at t = 5 h, a new peak at 13.3° emerges, corresponding to formation of the (100) plane of the hexagonal phase of the $CsCdBr_3$ perovskite. The complete conversion of the precursors into pure $CsCdBr_3$ perovskite occurs within 12 h.

During the investigation of the impact of the A site on the synthesis of $CsPbBr_3$, we observed that the initial formation of the $CsPbBr_3$ perovskite occurs within 1 h. However, in the case of $CsCdBr_3$, the formation of the perovskite takes a significantly longer time (t = 5 h).

https://doi.org/10.1021/acs.chemmater.3c01440
Chem. Mater. 2023, 35, 8909−8921

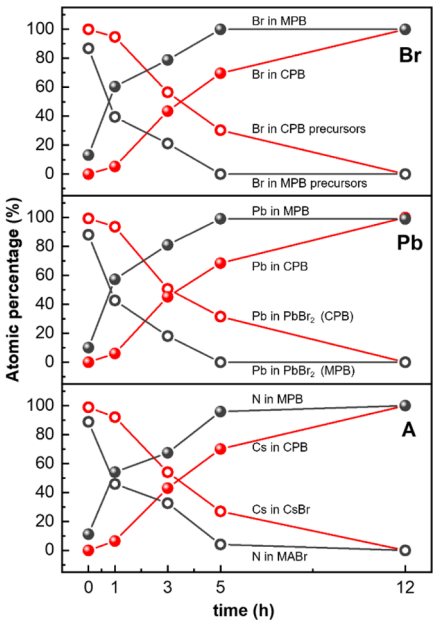

Figure 4. Atomic percentages of MA, Pb, and Br in $MAPbBr_3$ precursors and perovskites as a function of time (black) and atomic percentages of Cs, Pb, and Br in $CsPbBr_3$ precursors and perovskites as a function of time (red).

The slower formation rate of $CsCdBr_3$ compared to $CsPbBr_3$ can be attributed to two critical factors. First, hexagonal $CsCdBr_3$ has a higher formation energy (−1.477 eV/atom) compared to that of orthorhombic $CsPbBr_3$ (−1.517 eV/atom). These values are calculated using density functional theory (DFT) and obtained from the open quantum materials database (OQMD).[81,82] Second, the Cd−Br bond in $CsCdBr_3$ is weaker, with a bond dissociation energy of 159 kJ/mol,[83] while the Pb−Br bond in $CsPbBr_3$ is stronger, with a bond dissociation energy of 201 kJ/mol.[84] Importantly, the $[BX_3]^-$ octahedral network in the perovskite structure consists of $[BX_6]^{4-}$ units. The higher bond dissociation energy of Pb−Br with respect to Cd−Br promotes the formation and stability of $[PbBr_6]^{4-}$ units within the perovskite structure, rather than $[CdBr_6]^{4-}$ units. The higher stability of the products makes them less likely to revert back to the original reactants, which in turn leads to a higher formation rate of the desired product.

The observation that $CsCdBr_3$ takes longer to form (t = 5 h) compared to $CsPbBr_3$ (t = 1 h), followed by a similar time required for both compositions to achieve complete conversion to pure perovskite (t = 12 h), suggests that Cs^+ ions might diffuse at a comparable rate within the $[CdBr_3]^-$ chain networks as they do within the cuboctahedra $[PbBr_3]^-$ network to complete their respective perovskite structures. Therefore, the formation of the $[BX_6]^{4-}$ octahedral units could potentially be the rate-determining step that makes a difference in the overall reaction process. These observations indicate that a higher B-X bond dissociation energy in the $[BX_6]^{4-}$ octahedral units and a lower formation energy of the perovskite contribute to a higher rate of perovskite formation.

Figure 5a shows the XPS spectra for Cs $3d_{5/2}$, Cd 3d, and Br 3d regions for ball-milled $CsCdBr_3$ samples as a function of time. The deconvolution of the Cs $3d_{5/2}$ peak area shows a pattern similar to that observed in the $CsPbBr_3$ system, which was previously discussed in detail. At t = 0 h, only a single peak at Cd $3d_{3/2}$ regions is observed at 412.74 eV. This is attributed to the presence of Cd in the $CdBr_2$ precursor.[85] At t = 5 h, a new peak at 413.52 eV appears. According to previous studies[9,86] and the observations from Figure 1c, this new peak is ascribed to the inclusion of Cd into the perovskite structure. In other words, this peak is attributed to the integration of Cd atoms into the $[CdBr_3]^-$ framework of hexagonal $CsCdBr_3$ perovskites.

The behavior of Bromine (Br) in $CsCdBr_3$ samples closely follows the observations discussed in the $CsPbBr_3$ and $MAPbBr_3$ systems, as previously discussed.

Figure 6 illustrates the compositional XPS analysis for the two B-sites (Pb, Cd). For the $CsCdBr_3$ system, regardless of the elements present in the A, B, and X sites, the precursors remain unreacted for the first 3 h. Conversely, in $CsPbBr_3$ samples, the quantities of the elements in precursors progressively decrease at an early stage (t = 1 h) as the perovskite begins to form.

A surprising observation is that both the $CsCdBr_3$ and $CsPbBr_3$ samples undergo complete conversion of all elements into perovskite structures simultaneously, at an identical time of t = 12 h. Once the $[CdBr_3]^-$ framework starts to form, Cs^+ ions diffuse within the face-sharing chain of the $[CdBr_3]^-$ octahedral network at a similar rate to their diffusion within the corner-sharing $[PbBr_3]^-$ networks to make a complete ABX_3 perovskite structure. This resulted in the simultaneous formation of pure $CsCdBr_3$ and $CsPbBr_3$ perovskites. As a result, we can conclude that the difference in the formation rate of the $[BX_3]^-$ network plays a determinant role in governing the kinetics of perovskite formation.

Role of X-Site Components Br and Cl in the $CsPbX_3$ System. This section discusses the impact of halogens in ball-milled systems. The XRD results of the precursors for $CsPbCl_3$ at different milling times are shown in Figure 1d. For t = 0 h, the XRD patterns correspond to the initial precursors (CsCl and $PbCl_2$). After 1 h of reaction, the precursor peaks decrease in intensity and a new peak emerges at 15.81°. This peak corresponds to the (100) plane of the orthorhombic phase of $CsPbCl_3$. Interestingly, XRD analysis shows complete conversion of precursors into $CsPbCl_3$ perovskite after 5 h, which is considerably faster than that of $CsPbBr_3$ (12 h).

The faster reaction rate of $CsPbCl_3$ compared to that of $CsPbBr_3$ can be attributed to three critical factors. First, the smaller size of Cl^- ions relative to Br^- ions facilitates their mobility, allowing them to interact and bond with the $PbCl_2$ precursor more effectively. Second, the bonding between Pb^{2+} and Cl^- exhibits a stronger ionic character compared to the bonding between Pb^{2+} and Br^-. This leads to the more favorable formation of the $[PbCl_3]^-$ network and, consequently, the complete perovskite structure. Third, $CsPbCl_3$ possesses a lower formation energy (−1.745 eV/atom) compared to that of $CsPbBr_3$ (−1.517 eV/atom), which also contributes to a faster conversion time.

In addition to the B-site, the X-site also plays a key role in determining the formation rate of $[BX_6]^{4-}$ units in perovskites. Stronger bonding between B and X, along with smaller size of X^- ions, and a lower formation energy of the resulting perovskite, contribute to an accelerated formation rate of $[BX_6]^{4-}$ units. This favorable combination of factors facilitates the complete conversion of precursors to the desired perovskite phase.

The XPS results for the Cs $3d_{5/2}$, Pb 4f, and Cl 2p regions of the ball-milled $CsPbCl_3$ precursors at different milling times are shown in Figure 5b. The Cs $3d_{5/2}$ and Pb 4f regions in

https://doi.org/10.1021/acs.chemmater.3c01440
Chem. Mater. 2023, 35, 8909−8921

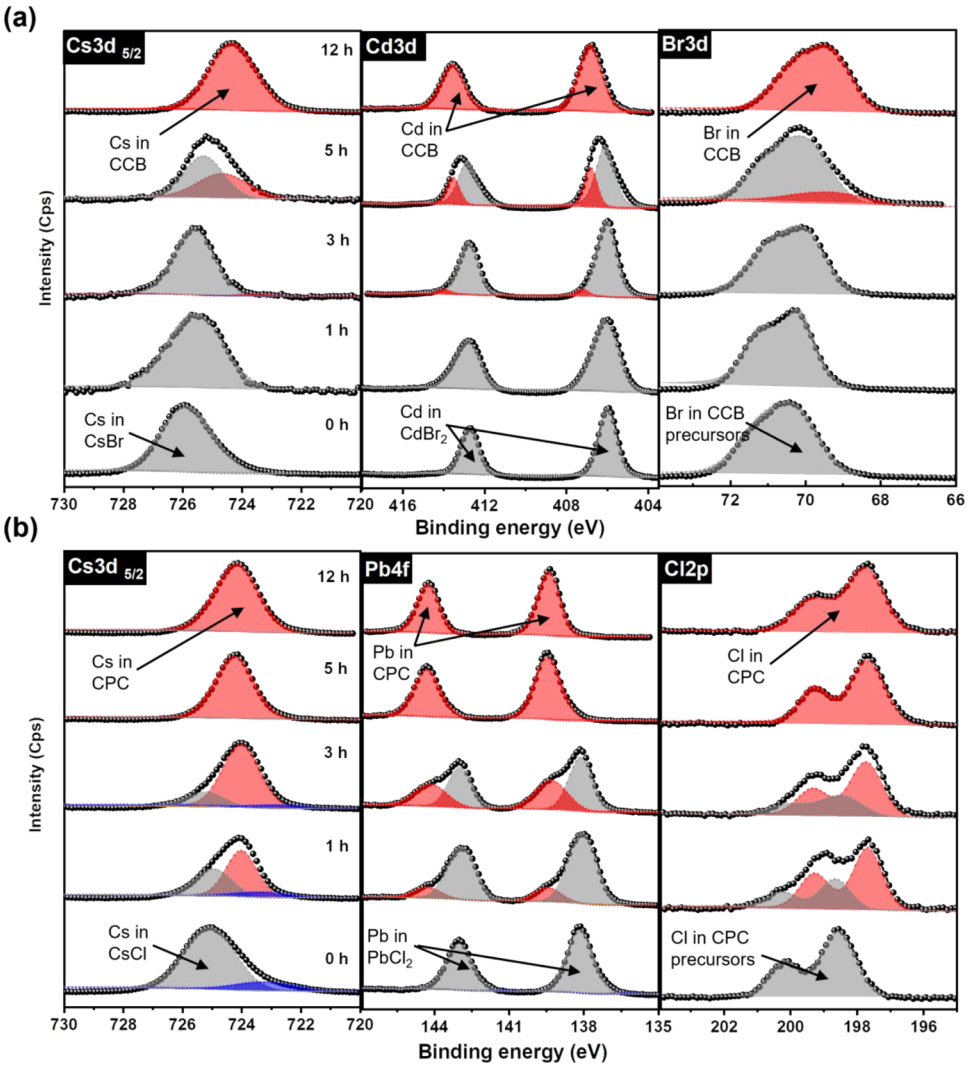

Figure 5. XPS results of ball-milled $CsCdBr_3$ (a) and $CsPbCl_3$ (b) precursors for different times. The red peaks correspond to the perovskites, and the gray peaks correspond to the precursors.

$CsPbCl_3$ show bands that align with those observed in $CsPbBr_3$ for both the precursors and the perovskites. The Cl 2p region corresponds to the X-site in the $CsPbCl_3$ perovskites. At t = 0 h, the band at 199.30 eV is attributed to the Cl in the CsCl and $PbCl_2$ precursors. As the perovskite formation progresses, a new band emerges at 198.5 eV, corresponding to the presence of Cl in $CsPbCl_3$ perovskites. XPS analysis confirmed full conversion of precursors into pure $CsPbCl_3$ perovskites at t = 5 h, as demonstrated by the single band centered at 198.5 eV. This is consistent with the observations from the XRD analysis.

Figure 7 is used to discuss the composition of the samples derived from the XPS results with a focus on the influence of Br and Cl. The figure shows that a significant amount of Cs, Pb, and Cl atoms (approximately 60%) in the $CsPbCl_3$ precursors undergo conversion into the perovskite structure after reaction for 1 h of reaction. In contrast, for $CsPbBr_3$ precursors, only about 10% of its elements convert to the $CsPbBr_3$ perovskite structure at t = 1 h. Furthermore, consistent with the previously discussed XRD results, the atomic percentages of Cs, Pb, and Cl elements after 5 h of reaction indicate complete conversion of the precursors into $CsPbCl_3$ samples, which is significantly faster than that of $CsPbBr_3$ (t = 12 h). This further highlights the importance of the B-X bond energy within the $[BX_6]^{4-}$ octahedral units, the formation energy of the resulting perovskite, and the size of the X^- ions in determining the rate of $[BX_3]^-$ network formation during the perovskite synthesis.

Perovskite Morphology Evolution. Figure 8 shows the (FESEM) images of the initial precursors for $CsPbBr_3$ (a), $CsPbCl_3$ (b), $CsCdBr_3$ (c), and $MAPbBr_3$ (d) followed by the corresponding images after full perovskite conversion (Figures 8e–h). The precursor morphologies of $CsPbBr_3$, $MAPbBr_3$, $CsPbCl_3$, and $CsCdBr_3$ predominantly exhibit large particles with varying shapes. However, upon complete conversion into perovskite, the observed morphological changes reveal a narrower area distribution for the grains across all of the investigated perovskite systems.

Figure 8i shows the area distributions for the precursors and perovskite structures. The particles of the precursors that have not been subjected to ball milling exhibit a wide range of particle areas. However, after the precursors are ball-milled and the perovskite structure is formed, the area distribution becomes much narrower. For all perovskite structures studied ($CsPbBr_3$, $CsPbCl_3$, $CsCdBr_3$, and $MAPbBr_3$), the grain areas are consistently within 1 $\mu m^2 < a < 3$ μm^2. The narrowing area

https://doi.org/10.1021/acs.chemmater.3c01440
Chem. Mater. 2023, 35, 8909–8921

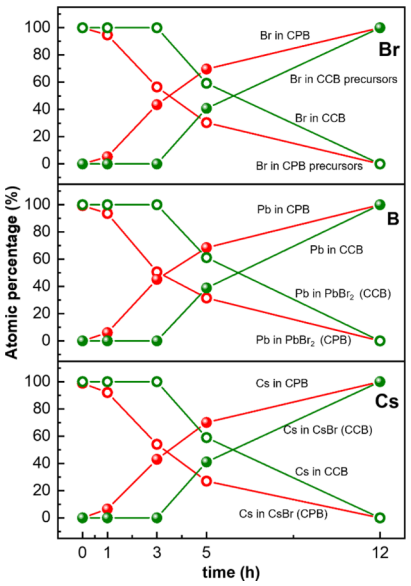

Figure 6. Atomic percentages of Cs, Cd, and Br in $CsCdBr_3$ precursors and perovskites as a function of time (green) and atomic percentages of Cs, Pb, and Br in $CsPbBr_3$ precursors and perovskites as a function of time (red).

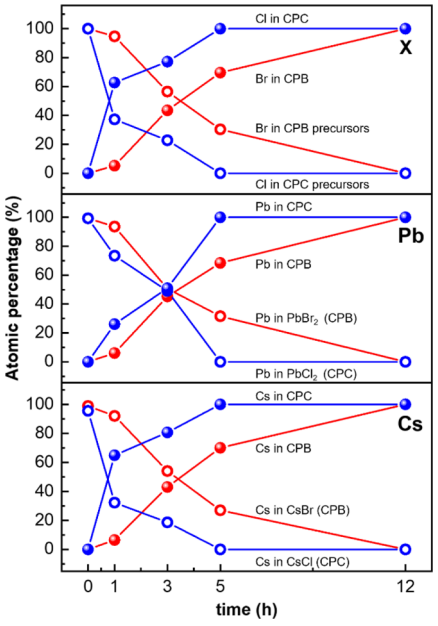

Figure 7. Atomic percentages of Cs, Pb, and Cl in $CsPbCl_3$ precursors and perovskites as a function of time (blue lines) and the atomic percentages of Cs, Pb, Br in $CsPbBr_3$ precursors and perovskites as a function of time (red lines).

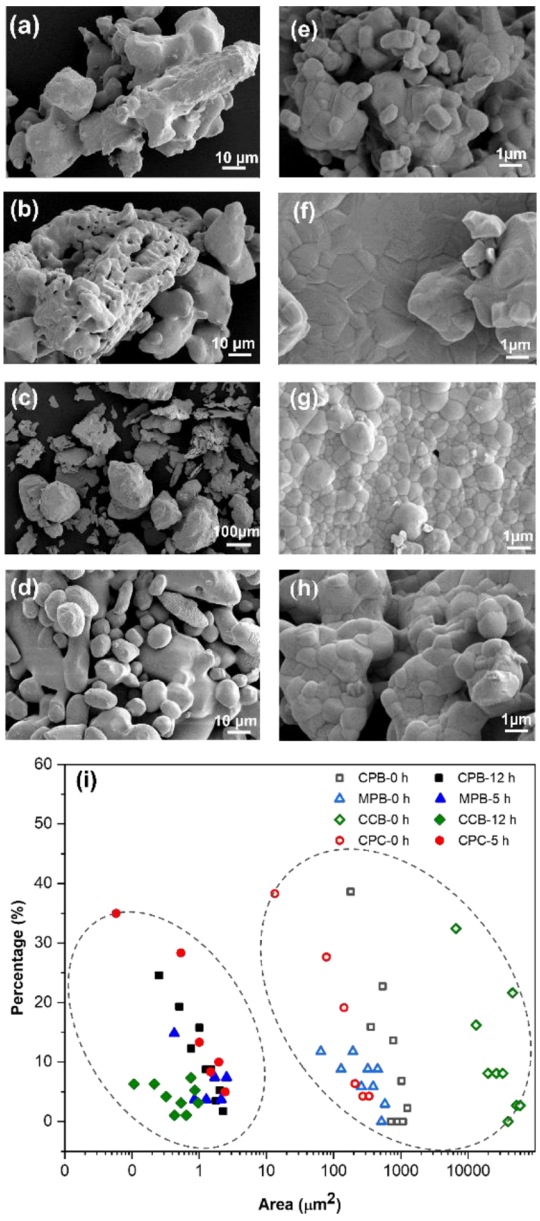

Figure 8. FESEM images of the nonball milled precursor for $CsPbBr_3$ (a), $MAPbCl_3$ (b), $CsCdBr_3$ (c), and $CsPbCl_3$ (d). FESEM images of pure $CsPbBr_3$ (e), $MAPbBr_3$ (f), $CsCdBr_3$ (g), and $CsPbCl_3$ (h) perovskites. Area distribution analysis of nonball milled $CsPbBr_3$, $MAPbBr_3$, $CsCdBr_3$, and $CsPbCl_3$ precursors, and their perovskite structures. (i) The larger oval represents a wide area distribution in precursors and the smaller oval represents a narrow area distribution in the pure perovskites.

distribution suggests that ball milling helps achieve uniform grain sizes and promotes the formation of homogeneous perovskite structures.

Proposed Mechanism. Based on the results discussed, a mechanism is proposed for the solid-state synthesis of the studied halide perovskites. The suggested mechanism is based on the chemical composition and crystalline structure derived from the systematic interchange of the A, B, and X sites within the ABX_3 halide perovskite structure. Figure 9 illustrates the proposed mechanism of $CsPbBr_3$, $MAPbBr_3$, and $CsPbCl_3$, which form an orthorhombic crystalline structure at room temperature. Figure 10, on the other hand, depicts the formation mechanism of $CsCdBr_3$, which is primarily known for forming a hexagonal structure at room temperature.[67,68] The mechanisms comprise four distinct steps, each of which is elucidated and discussed next.

(I) A−X bond dissociation: This is the initial step in the reaction and involves the dissociation of A−X bonds during the milling of the precursors. As illustrated in Figure 9, the structure of BX_2 ($PbCl_2$ or $PbBr_2$) precursors exhibits a seven-coordinated lead(II) ion arrangement, coordinating with either chlorine (Cl^-) or bromine (Br^-) ions. This results in an orthorhombic crystalline structure with a *Pnma* space group.

https://doi.org/10.1021/acs.chemmater.3c01440
Chem. Mater. 2023, 35, 8909−8921

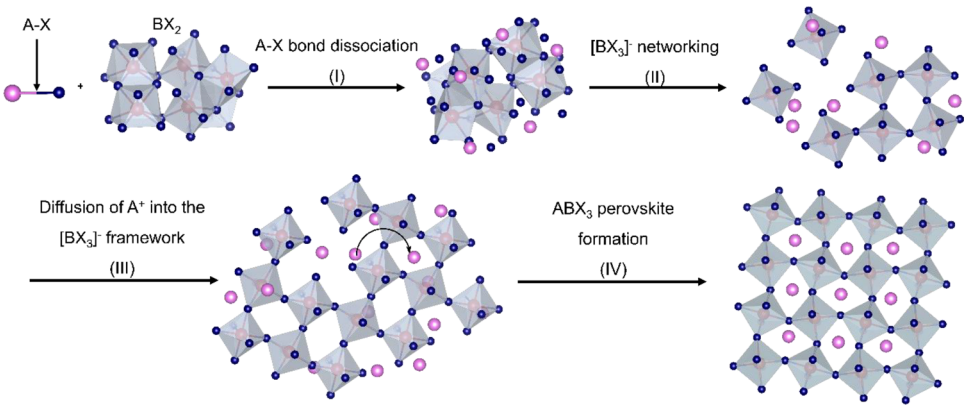

Figure 9. Proposed mechanism for the ball-milling synthesis of $CsPbBr_3$, $MAPbBr_3$, and $CsPbCl_3$ perovskites. The A (Cs, MA), B (Pb), and X (Br, Cl) sites are colored pink, red, and blue, respectively.

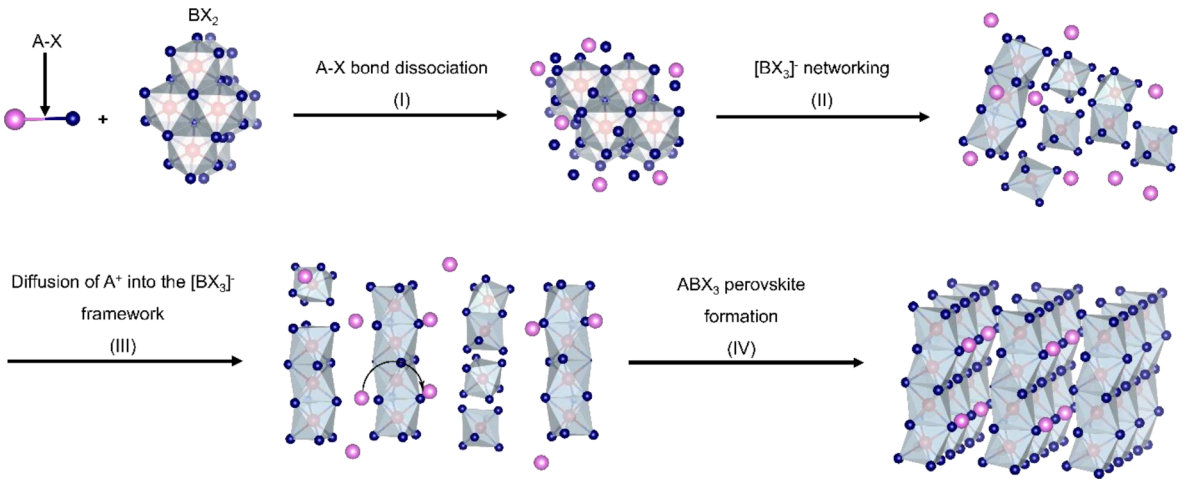

Figure 10. Proposed mechanism for the ball-milling synthesis of $CsCdBr_3$ perovskites. The A (Cs), B (Cd), and X (Br) sites are colored pink, red, and blue, respectively.

Detailed examination of their space group reveals that depending on the halogen used, the asymmetric unit cell comprises either $PbCl_2$ or $PbBr_2$. As a result, the BX_2 ($PbBr_2$ or $PbCl_2$) precursors lack sufficient halogens (X) to establish the desired octahedral network, necessitating the introduction of additional halogens into the BX_2 structure. Given that the reaction takes place in the solid state, only the two precursors (A−X and BX_2) are available in the reaction environment. Therefore, the breakage of the A−X bond is the sole source for BX_2 to obtain the supplementary halogens. Furthermore, achieving a complete perovskite crystalline structure requires the presence of the A cations, necessitating the breaking of the A−X bond and producing separate ions. As mentioned in the role of the A-site, $MAPbBr_3$ perovskites form faster than $CsPbBr_3$. This discrepancy is attributed to the difference in the bond strength between MA−Br and Cs−Br bonds. The weaker MA−Br bond initiates the reaction at an earlier stage, leading to the accelerated formation of the $MAPbBr_3$ perovskite structure.

(II) $[BX_3]^-$ octahedral network formation: Once sufficient halogens are available, a structural transformation occurs in the orthorhombic BX_2 compound. In this process, Pb (II) ions undergo migration and reorganization, coordinated with six halide ligands to create octahedral $[PbBr_6]^{4-}$ units. Eventually, these units come together in a corner-sharing manner to form a $[BX_3]^-$ octahedral framework. In the context of the role of X^-site, it is observed that pure $CsPbCl_3$ is obtained after 5 h, whereas obtaining pure $CsPbBr_3$ requires 12 h. This can be attributed to the higher bond energy of Pb−Cl compared to Pb−Br, combined with the smaller size of Cl^- compared to Br^-. The higher bond energy in the product leads to a more stable product and reduces the possibility of reverting back to the initial precursors. As a result, these factors collectively make the transformation to the octahedral network easier for $CsPbCl_3$ compared to $CsPbBr_3$.

(III) Diffusion of the A^+ cations into the octahedral network: After the structural transformation of BX_2 into the octahedral network, the A cations start diffusing within the cuboctahedra spaces of the $[BX_3]^-$ network, as depicted in Figure 9. This diffusion process is influenced by factors that affect the diffusion rate of A^+ cations within the octahedral network including molecular weight, size, concentration, and temperature. As previously explained, the initial formation of $MAPbBr_3$ perovskite occurs faster compared to $CsPbBr_3$. Furthermore, complete perovskite formation of $MAPbBr_3$ is observed after only 5 h, which is significantly shorter than the time required for $CsPbBr_3$ formation (12 h). In addition to the previously discussed difference in the bond energy of MABr compared to CsBr, this variation can also be attributed to the higher diffusion rate of MA cations compared to Cs cations, which is primarily due to the lower molecular weight of the MA cation.

https://doi.org/10.1021/acs.chemmater.3c01440
Chem. Mater. 2023, 35, 8909−8921

(IV) ABX_3 perovskite formation: The primary role of the A cation in the ABX_3 perovskite structure is to provide charge balance and structural stability to the $[BX_3]^-$ octahedral network. Once the diffusion of A cations is complete, a pure ABX_3 perovskite structure is achieved. The time required to obtain different perovskites varies due to the different formation energies associated with each perovskite. These formation energies directly impact the stability of the resulting perovskites. Consequently, they determined the time required to achieve pure perovskite structures.

Figure 10 illustrates the formation mechanism of the hexagonal $CsCdBr_3$ perovskite structure. While the primary steps for the formation of this structure are the same as those in Figure 9, the resulting structure is characterized by a one-dimensional hexagonal crystalline arrangement.

$CdBr_2$ crystallizes into a trigonal structure with the space group $\bar{R}3m$.[87] Upon the breakage of the A-X bond, a structural transformation occurs from the trigonal arrangement to a face-sharing octahedral network of $[CdBr_3]^-$. This network extends infinitely along the crystallographic *c*- axis, resulting in a one-dimensional perovskite structure.[88] The distance between Cd atoms within the $[CdBr_3]^-$ chain is much shorter than the distance between Cd atoms in different chains, thus giving rise to this one-dimensional characteristic.

Since the $[CdBr_3]^-$ chains are anionic, Cs cations need to diffuse between the chains to provide charge balance and structural stability to the anionic framework. Once the diffusion process is completed, a complete one-dimensional hexagonal structure of $CsCdBr_3$ is formed.

CONCLUSIONS

In conclusion, our research aimed to investigate the kinetics and mechanisms underlying the solid-state synthesis of halide perovskites. To conduct this study, we utilized a $CsPbBr_3$ system (ABX_3) as a reference to study the exchange of A, B, and X sites with methylammonium (MA^+), Cd^{2+}, and Cl^-, respectively. First, through meticulous optimization of the milling time, we successfully produced pure gram-scale $CsPbBr_3$, $MAPbBr_3$, $CsCdBr_3$, and $CsPbCl_3$. These perovskite materials demonstrated remarkable phase stability when exposed to air and an average humidity of 48.5% for 21 consecutive days.

To gain insights into the kinetics and formation mechanisms of the halide perovskites, we utilized various analytical techniques, including XPS, XRD, FESEM, UV−vis, and PL which provided valuable information about crystalline structure, morphology, and spectroscopic characteristics of the samples over time. XPS proved to be especially invaluable in monitoring reaction kinetics and mechanisms, offering insights into the conversion rate of precursors to perovskites, material purity, and chemical shifts. These findings can serve as a reference for future studies involving more intricate halide perovskite compositions.

This investigation underscores the importance of key factors, such as the bond energy of the AX precursor, perovskite formation energy, the diffusion rate of "A" cations, and B-X bond energy within the $[BX_3]^-$ framework, in influencing the kinetics and mechanisms of halide perovskite formation during solid-state synthesis. Based on the data collected, we proposed a plausible mechanism for the ball-milling synthesis, involving four phases: (I) precursor dissociation, (II) $[BX_3]^-$ octahedral network formation, (III) diffusion of the A^+ cations into the octahedral network, and (IV) ABX_3 perovskite formation. The outcomes of this study not only provide insights into the intricate kinetics and mechanisms governing the room-temperature solid-state synthesis of halide perovskites but also open avenues to fine-tune the synthesis process and enhance the material quality for more complex halide perovskite compositions using this methodology.

ASSOCIATED CONTENT

Supporting Information

The Supporting Information is available free of charge at https://pubs.acs.org/doi/10.1021/acs.chemmater.3c01440.

> XRD of $CsPbBr_3$ ball-milled precursors as a function of time along with the reference patterns of $CsPb_2Br_5$ and Cs_4PbBr_6; time-dependent reflectance spectra of ball-milled $CsPbBr_3$, $MAPbBr_3$, $CsCdBr_3$, and $CsPbCl_3$ precursors; plot of $(F(R)h\nu)^2$(eV $cm^{1-})^2$ versus energy (eV) derived from the UV−vis DRS spectra for band gap calculation in (a) $CsPbBr_3$, (b) $MAPbBr_3$, (c) $CsCdBr_3$, and (d) $CsPbCl_3$ samples; PL spectra of $CsPbBr_3$ and $MAPbBr_3$ samples; XRD of (a) $CsPbBr_3$, (b) $MAPbBr_3$, (c) $CsCdBr_3$, and (d) $CsPbCl_3$ stored in the glovebox at day 0 (fresh sample) and after 1 year; and XRD of (a) $CsPbBr_3$, (b) $MAPbBr_3$, (c) $CsCdBr_3$, and (d) $CsPbCl_3$ during a 21-day exposure to an average humidity of 48% and an average temperature of 21.3 °C (PDF)

AUTHOR INFORMATION

Corresponding Author

Manuel A. Quevedo-Lopez − *Department of Material Science & Engineering, The University of Texas at Dallas, Richardson, Texas 75080, United States;* orcid.org/0000-0002-1867-7584; Email: mquevedo@utdallas.edu

Authors

Mahsa Shekarnoush − *Department of Material Science & Engineering, The University of Texas at Dallas, Richardson, Texas 75080, United States; Department of Chemistry and Biochemistry, The University of Texas at Dallas, Richardson, Texas 75080, United States;* orcid.org/0000-0003-0878-7410

Leunam Fernandez-Izquierdo − *Department of Material Science & Engineering, The University of Texas at Dallas, Richardson, Texas 75080, United States*

Francisco S. Aguirre-Tostado − *Department of Material Science & Engineering, The University of Texas at Dallas, Richardson, Texas 75080, United States; Unidad Monterrey, Parque de Investigación e Innovación Tecnológica, Centro de Investigación en Materiales Avanzados, S. C. (CIMAV), Apodaca, Nuevo León 66628, Mexico; Centro de Investigación en Materiales Avanzados, S. C. (CIMAV), Unidad Monterrey, Apodaca, Nuevo León 66628, Mexico;* orcid.org/0000-0002-8721-0179

Zeshaan H. Shamsi − *Department of Material Science & Engineering, The University of Texas at Dallas, Richardson, Texas 75080, United States;* orcid.org/0009-0002-0113-4417

Complete contact information is available at: https://pubs.acs.org/10.1021/acs.chemmater.3c01440

https://doi.org/10.1021/acs.chemmater.3c01440
Chem. Mater. 2023, 35, 8909−8921

Author Contributions

The manuscript was written through the contributions of all authors. All authors have given approval to the final version of the manuscript.

Notes

The authors declare no competing financial interest.

■ ACKNOWLEDGMENTS

The authors would like to express their gratitude to the Texas Instruments University Chair in Nanoelectronics at the University of Texas at Dallas for their support and funding. F.S. Aguirre-Tostado wants to acknowledge partial financial support from Conahcyt Mexico.

■ ABBREVIATIONS

CPB, $CsPbBr_3$; MPB, $MAPbBr_3$; CCB, $CsCdBr_3$; CPC, $CsPbCl_3$

■ REFERENCES

(1) Akkerman, Q. A.; Manna, L. What Defines a Halide Perovskite? *ACS Energy Lett.* **2020**, *5*, 604−610.
(2) Hoefler, S. F.; Trimmel, G.; Rath, T. Progress on lead-free metal halide perovskites for photovoltaic applications: a review. *Monatsh. Chem.* **2017**, *148*, 795−826.
(3) Lim, D.-H.; Ramasamy, P.; Kwak, D.-H.; Lee, J.-S. Solution-Phase Synthesis of Rubidium Lead Iodide Orthorhombic Perovskite Nanowires. *Nanotechnology* **2017**, *28*, 255601.
(4) Abdin, Z. Ul; Qasim, I.; Malik, M. I.; Rashid, M. Experimental and Numerical Investigations on Feasibility of Inorganic $KSnCl_3$ Perovskite Absorber and SWCNT-HTL for Solar Cells. *Heliyon* **2023**, *9*, No. e14802.
(5) Pérez-Osorio, M. A.; Lin, Q.; Phillips, R. T.; Milot, R. L.; Herz, L. M.; Johnston, M. B.; Giustino, F. Raman Spectrum of the Organic−Inorganic Halide Perovskite $CH_3NH_3PbI_3$ from First Principles and High-Resolution Low-Temperature Raman Measurements. *J. Phys. Chem. C* **2018**, *122*, 21703−21717.
(6) Zhumekenov, A. A.; Saidaminov, M. I.; Haque, M. A.; Alarousu, E.; Sarmah, S. P.; Murali, B.; Dursun, I.; Miao, X.-H.; Abdelhady, A. L.; Wu, T.; Mohammed, O. F.; Bakr, O. M. Formamidinium Lead Halide Perovskite Crystals with Unprecedented Long Carrier Dynamics and Diffusion Length. *ACS Energy Lett.* **2016**, *1*, 32−37.
(7) Uribe, J. I.; Ramirez, D.; Osorio-Guillén, J. M.; Osorio, J.; Jaramillo, F. $CH_3NH_3CaI_3$ Perovskite: Synthesis, Characterization, and First-Principles Studies. *J. Phys. Chem. C* **2016**, *120*, 16393−16398.
(8) Ni, H. F.; Ye, L. K.; Zhuge, P. C.; Hu, B. L.; Lou, J. R.; Su, C. Y.; Zhang, Z. X.; Xie, L. Y.; Fu, D. W.; Zhang, Y. A nickel (ii)-based one-dimensional organic−inorganic halide perovskite ferroelectric with the highest Curie temperature. *Chem. Sci.* **2023**, *14*, 1781−1786.
(9) Guo, J.; Hu, Q.; Lu, M.; Li, A.; Zhang, X.; Sheng, R.; Chen, P.; Zhang, Y.; Wu, J.; Fu, Y.; Sun, G.; Yu, W. W.; Bai, X. Pb^{2+} Doped $CsCdBr_3$ Perovskite Nanorods for Pure-Blue Light-Emitting Diodes. *Chem. Eng. J.* **2022**, *427*, No. 131010.
(10) Brynestad, J.; Yakel, H. L.; Smith, G. P. Temperature Dependence of the Absorption Spectrum of Nickel (II)-Doped $KMgCl_3$ and the Crystal Structure of $KMgCl_3$. *J. Chem. Phys.* **1966**, *45*, 4652−4664.
(11) Körbel, S.; Marques, M. A. L.; Botti, S. Stable Hybrid Organic−Inorganic Halide Perovskites for Photovoltaics from Ab Initio High-Throughput Calculations. *J. Mater. Chem. A* **2018**, *6*, 6463−6475.
(12) Bartel, C. J.; Sutton, C.; Goldsmith, B. R.; Ouyang, R.; Musgrave, C. B.; Ghiringhelli, L. M.; Scheffler, M. New Tolerance Factor to Predict the Stability of Perovskite Oxides and Halides. *Sci. Adv.* **2019**, *5*, No. eaav0693.
(13) Nishat, M.; Hossain, Md. K.; Hossain, Md. R.; Khanom, S.; Ahmed, F.; Hossain, Md. A. Role of Metal and Anions in Organo-Metal Halide Perovskites $CH_3NH_3MX_3$ (M: Cu, Zn, Ga, Ge, Sn, Pb; X: Cl, Br, I) on Structural and Optoelectronic Properties for Photovoltaic Applications. *RSC Adv.* **2022**, *12*, 13281−13294.
(14) Hasan, N.; Arifuzzaman, M.; Kabir, A. Structural, Elastic and Optoelectronic Properties of Inorganic Cubic $FrBX_3$ (B = Ge, Sn; X = Cl, Br, I) Perovskite: The Density Functional Theory Approach. *RSC Adv.* **2022**, *12*, 7961−7972.
(15) Procida, G.; Schier, R.; Valencia, A. M.; Cocchi, C. First-Principles Analysis of the Optical Properties of Lead Halide Perovskite Solution Precursors. *Phys. Chem. Chem. Phys.* **2021**, *23*, 21087−21096.
(16) Li, C.; Lu, X.; Ding, W.; Feng, L.; Gao, Y.; Guo, Z. Formability of ABX_3 (X = F, Cl, Br, I) Halide Perovskites. *Acta Crystallogr., Sect. B: Struct. Sci., Cryst. Eng. Mater.* **2008**, *64*, 702−707.
(17) Goldschmidt, V. M. Die Gesetze der Krystallochemie. *Naturwissenschaften* **1926**, *14*, 477−485.
(18) Manser, J. S.; Christians, J. A.; Kamat, P. V. Intriguing Optoelectronic Properties of Metal Halide Perovskites. *Chem. Rev.* **2016**, *116*, 12956−13008.
(19) Wang, R.; Huang, T.; Xue, J.; Tong, J.; Zhu, K.; Yang, Y. Prospects for Metal Halide Perovskite-Based Tandem Solar Cells. *Nat. Photonics* **2021**, *15*, 411−425.
(20) Ahmad, S.; George, C.; Beesley, D. J.; Baumberg, J. J.; De Volder, M. Photo-Rechargeable Organo-Halide Perovskite Batteries. *Nano Lett.* **2018**, *18*, 1856−1862.
(21) Zhang, Q.; Shang, Q.; Su, R.; Do, T. T. H.; Xiong, Q. Halide Perovskite Semiconductor Lasers: Materials, Cavity Design, and Low Threshold. *Nano Lett.* **2021**, *21*, 1903−1914.
(22) Zhou, Y.; Chen, J.; M. Bakr, O.; Omar, F. M. Metal Halide Perovskites for X-ray Imaging Scintillators and Detectors. *ACS Energy Lett.* **2021**, *6*, 739−768.
(23) Li, Z.; Zhou, F.; Yao, H.; Ci, Z.; Yang, Z.; Jin, Z. Halide Perovskites for High-Performance X-Ray Detector. *Mater. Today* **2021**, *48*, 155−175.
(24) Faridi, A. W.; Imran, M.; Tariq, G. H.; Ullah, S.; Noor, S. F.; Ansar, S.; Sher, F. Synthesis and Characterization of High-Efficiency Halide Perovskite Nanomaterials for Light-Absorbing Applications. *Ind. Eng. Chem. Res.* **2023**, *62*, 4494−4502.
(25) Ou, Q.; Bao, X.; Zhang, Y.; Shao, H.; Xing, G.; Li, X.; Shao, L.-Y.; Bao, Q. Band Structure Engineering in Metal Halide Perovskite Nanostructures for Optoelectronic Applications. *Nano Mater. Sci.* **2019**, *1*, 268.
(26) Zhang, X.; Liu, J.; Song, Z.; Zuo, W.; Fan, Z.; He, X.; Luo, K.; Ye, Q.; Liao, C. Tuning Bandgap of Mixed-Halide Perovskite for Improved Photovoltaic Performance Under Monochromatic-Light Illumination. *Phys. Status Solidi A* **2019**, *216*, No. 1800727.
(27) Herz, L. M. Charge-Carrier Mobilities in Metal Halide Perovskites: Fundamental Mechanisms and Limits. *ACS Energy Lett.* **2017**, *2*, 1539−1548.
(28) Dong, Q.; Fang, Y.; Shao, Y.; Mulligan, P.; Qiu, J.; Cao, L.; Huang, J. Electron-Hole Diffusion Lengths > 175 Mm in Solution-Grown $CH_3NH_3PbI_3$ Single Crystals. *Science* **2015**, *347*, 967−970.
(29) Fan, K.; Chan, C. C. S.; Yuan, L.; Yan, K.; Wong, K. S. New Insights into Hot-Charge Relaxation in Lead Halide Perovskite: Dynamical Bandgap Change, Hot-Biexciton Effect, and Photo-Bleaching Shift. *ACS Photonics* **2022**, *9*, 2304−2314.
(30) Liu, J.; Qu, J.; Kirchartz, T.; Song, J. Optoelectronic Devices Based on the Integration of Halide Perovskites with Silicon-Based Materials. *J. Mater. Chem. A* **2021**, *9*, 20919−20940.
(31) Zhang, Y.; Siegler, T. D.; Thomas, C. J.; Abney, M. K.; Shah, T.; De Gorostiza, A.; Greene, R. M.; Korgel, B. A. A "Tips and Tricks" Practical Guide to the Synthesis of Metal Halide Perovskite Nanocrystals. *Chem. Mater.* **2020**, *32*, 5410−5423.
(32) Hossain, A.; Bandyopadhyay, P.; Karmakar, A.; Ullah, A. K. M. A.; Manavalan, R. K.; Sakthipandi, K.; Alhokbany, N.; Alshehri, S. M.; Ahmed, J. The Hybrid Halide Perovskite: Synthesis Strategies, Fabrications, and Modern Applications. *Ceram. Int.* **2022**, *48*, 7325−7343.
(33) Zheng, L.; Nozariasbmarz, A.; Hou, Y.; Yoon, J.; Li, W.; Zhang, Y.; Wu, H.; Yang, D.; Ye, T.; Sanghadasa, M.; Wang, K.; Poudel, B.;

https://doi.org/10.1021/acs.chemmater.3c01440
Chem. Mater. 2023, 35, 8909−8921

Priya, S.; Wang, K. A Universal All-Solid Synthesis for High Throughput Production of Halide Perovskite. *Nat. Commun.* **2022**, *13*, 7399.
(34) Ha, S.-T.; Su, R.; Xing, J.; Zhang, Q.; Xiong, Q. Metal Halide Perovskite Nanomaterials: Synthesis and Applications. *Chem. Sci.* **2017**, *8*, 2522−2536.
(35) Elsayed, M. R. A.; Elseman, A. M.; Abdelmageed, A. A.; Hashem, H. M.; Hassen, A. Green and Cost-Effective Morter Grinding Synthesis of Bismuth-Doped Halide Perovskites as Efficient Absorber Materials. *J. Mater. Sci. Mater. Electron.* **2023**, *34*, 194.
(36) Sadhukhan, P.; Kundu, S.; Roy, A.; Ray, A.; Maji, P.; Dutta, H.; Pradhan, S. K.; Das, S. Solvent-Free Solid-State Synthesis of High Yield Mixed Halide Perovskites for Easily Tunable Composition and Band Gap. *Cryst. Growth Des.* **2018**, *18*, 3428−3432.
(37) Huang, D.; Xie, P.; Pan, Z.; Rao, H.; Zhong, X. One-Step Solution Deposition of $CsPbBr_3$ Based on Precursor Engineering for Efficient All-Inorganic Perovskite Solar Cells. *J. Mater. Chem. A* **2019**, *7*, 22420−22428.
(38) Zhou, S. Rapid Separation and Purification of Lead Halide Perovskite Quantum Dots through Differential Centrifugation in Nonpolar Solvent. *RSC Adv.* **2021**, *11*, 28410−28419.
(39) Vighnesh, K.; Wang, S.; Liu, H.; Rogach, A. L. Hot-Injection Synthesis Protocol for Green-Emitting Cesium Lead Bromide Perovskite Nanocrystals. *ACS Nano* **2022**, *16*, 19618−19625.
(40) Nedelcu, G.; Protesescu, L.; Yakunin, S.; Bodnarchuk, M. I.; Grotevent, M. J.; Kovalenko, M. V. Fast Anion-Exchange in Highly Luminescent Nanocrystals of Cesium Lead Halide Perovskites ($CsPbX_3$, X = Cl, Br, I). *Nano Lett.* **2015**, *15*, 5635−5640.
(41) Rosales, B. A.; Men, L.; Cady, S. D.; Hanrahan, M. P.; Rossini, A. J.; Vela, J. Persistent Dopants and Phase Segregation in Organolead Mixed-Halide Perovskites. *Chem. Mater.* **2016**, *28*, 6848−6859.
(42) Yoon, S. J.; Stamplecoskie, K. G.; Kamat, P. V. How Lead Halide Complex Chemistry Dictates the Composition of Mixed Halide Perovskites. *J. Phys. Chem. Lett.* **2016**, *7*, 1368−1373.
(43) Rosales, B. A.; Hanrahan, M. P.; Boote, B. W.; Rossini, A. J.; Smith, E. A.; Vela, J. Lead Halide Perovskites: Challenges and Opportunities in Advanced Synthesis and Spectroscopy. *ACS Energy Lett.* **2017**, *2*, 906−914.
(44) Zhang, M.; Zheng, Z.; Fu, Q.; Chen, Z.; He, J.; Zhang, S.; Yan, L.; Hu, Y.; Luo, W. Growth and Characterization of All-Inorganic Lead Halide Perovskite Semiconductor $CsPbBr_3$ Single Crystals. *CrystEngComm* **2017**, *19*, 6797−6803.
(45) Ishigaki, T.; Seki, K.; Nishimura, E.; Watanabe, T.; Yoshimura, M. Melt Synthesis and Characterization of Complexed Oxide Perovskites Containing Rare Earths. *J. Alloys Compd.* **2006**, *408*, 1177−1181.
(46) Leupold, N.; Schötz, K.; Cacovich, S.; Bauer, I.; Schultz, M.; Daubinger, M.; Kaiser, L.; Rebai, A.; Rousset, J.; Köhler, A.; Schulz, P.; Moos, R.; Panzer, F. High Versatility and Stability of Mechanochemically Synthesized Halide Perovskite Powders for Optoelectronic Devices. *ACS Appl. Mater. Interfaces* **2019**, *11*, 30259−30268.
(47) Martínez-Sarti, L.; Palazon, F.; Sessolo, M.; Bolink, H. J. Dry Mechanochemical Synthesis of Highly Luminescent, Blue and Green Hybrid Perovskite Solids. *Adv. Opt. Mater.* **2020**, *8*, No. 1901494.
(48) Rosales, B. A.; Wei, L.; Vela, J. Synthesis and Mixing of Complex Halide Perovskites by Solvent-Free Solid-State Methods. *J. Solid State Chem.* **2019**, *271*, 206−215.
(49) Baek, K. Y.; Lee, W.; Lee, J.; et al. Mechanochemistry-driven engineering of 0D/3D heterostructure for designing highly luminescent Cs−Pb−Br perovskites. *Nat. Commun.* **2022**, *13*, 4263.
(50) Takacs, L. The Historical Development of Mechanochemistry. *Chem. Soc. Rev.* **2013**, *42*, 7649−7659.
(51) Palazon, F.; El Ajjouri, Y.; Bolink, H. J. Making by Grinding: Mechanochemistry Boosts the Development of Halide Perovskites and Other Multinary Metal Halides. *Adv. Energy Mater.* **2020**, *10*, No. 1902499.
(52) Hong, Z.; Tan, D.; John, R. A.; Tay, Y. K. E.; Ho, Y. K. T.; Zhao, X.; Sum, T. C.; Mathews, N.; García, F.; Soo, H. S. Completely Solvent-Free Protocols to Access Phase-Pure, Metastable Metal Halide Perovskites and Functional Photodetectors from the Precursor Salts. *iScience* **2019**, *16*, 312−325.
(53) Xing, T.; Sunarso, J.; Yang, W.; Yin, Y.; Glushenkov, A. M.; Li, L. H.; Howlett, P. C.; Chen, Y. Ball Milling: A Green Mechanochemical Approach for Synthesis of Nitrogen Doped Carbon Nanoparticles. *Nanoscale* **2013**, *5*, 7970−7976.
(54) Piras, C. C.; Fernández-Prieto, S.; Borggraeve, W. M. D. Ball Milling: A Green Technology for the Preparation and Functionalisation of Nanocellulose Derivatives. *Nanoscale Adv.* **2019**, *1*, 937−947.
(55) Palazon, F.; Ajjouri, Y. E.; Sebastia-Luna, P.; Lauciello, S.; Manna, L.; Bolink, H. J. Mechanochemical Synthesis of Inorganic Halide Perovskites: Evolution of Phase-Purity, Morphology, and Photoluminescence. *J. Mater. Chem. C* **2019**, *7*, 11406−11410.
(56) Karmakar, A.; Askar, A. M.; Bernard, G. M.; Terskikh, V. V.; Ha, M.; Patel, S.; Shankar, K.; Michaelis, V. K. Mechanochemical Synthesis of Methylammonium Lead Mixed−Halide Perovskites: Unraveling the Solid-Solution Behavior Using Solid-State NMR. *Chem. Mater.* **2018**, *30*, 2309−2321.
(57) López, C. A.; Abia, C.; Rodrigues, J. E.; Serrano-Sánchez, F.; Nemes, N. M.; Martínez, J. L.; Fernandez-Díaz, M. T.; Biškup, N.; Alvarez-Galván, C.; Carrascoso, F.; Castellanos-Gomez, A.; Alonso, J. A. Enhanced Stability in $CH_3NH_3PbI_3$ Hybrid Perovskite from Mechano-Chemical Synthesis: Structural Microstructural and Optoelectronic Characterization. *Sci. Rep.* **2020**, *10*, 11228.
(58) Prochowicz, D.; Yadav, P.; Saliba, M.; Saski, M.; M. Zakeeruddin, S.; Lewiński, J.; Grätzel, M. Mechanosynthesis of Pure Phase Mixed-Cation $MA_xFA_{1-x}PbI_3$ Hybrid Perovskites: Photovoltaic Performance and Electrochemical Properties. *Sustainable Energy Fuels* **2017**, *1*, 689−693.
(59) Prochowicz, D.; Yadav, P.; Saliba, M.; Kubicki, D. J.; Tavakoli, M. M.; Zakeeruddin, S. M.; Lewiński, J.; Emsley, L.; Grätzel, M. One-Step Mechanochemical Incorporation of an Insoluble Cesium Additive for High Performance Planar Heterojunction Solar Cells. *Nano Energy* **2018**, *49*, 523−528.
(60) Posudievsky, O. Yu.; Konoshchuk, N. V.; Karbivskyy, V. L.; Boiko, O. P.; Koshechko, V. G.; Pokhodenko, V. D. Structural and Spectral Characteristics of Mechanochemically Prepared $CsPbBr_3$. *Theor. Exp. Chem.* **2017**, *53*, 235−243.
(61) Kriegner, D.; Matěj, Z.; Kužel, R.; Holý, V. Powder Diffraction in Bragg−Brentano Geometry with Straight Linear Detectors. *J. Appl. Crystallogr.* **2015**, *48*, 613−618.
(62) Momma, K.; Izumi, F. VESTA 3 for Three-Dimensional Visualization of Crystal, Volumetric and Morphology Data. *J. Appl. Crystallogr.* **2011**, *44*, 1272−1276.
(63) Shannon, R. D. Revised Effective Ionic Radii and Systematic Studies of Interatomic Distances in Halides and Chalcogenides. *Acta Crystallogr., Sect. A: Found. Adv.* **1976**, *32*, 751−767.
(64) Natta, G.; Passerini, L. Isomorfismo, Polimorfismo e Morfotropia. I. Composti del Tipo ABX_3. *Gazz. Chim. Ital.* **1928**, *58*, 472−484.
(65) *Materials Data on CsCdBr3 by Materials Project; mp-570231; Lawrence Berkeley National Lab. (LBNL)*, LBNL Materials Project: Berkeley, CA (United States), 2020, DOI: 10.17188/1275593.
(66) Wang, X.; Zhao, Y.; Zeng, S.; Wang, Z.; Chen, Y.; Ni, J. Cubic Halide Perovskites as Potential Low Thermal Conductivity Materials: A Combined Approach of Machine Learning and First-Principles Calculations. *Phys. Rev. B* **2022**, *105*, No. 014310.
(67) Jia, W.; Wei, Q.; Ge, S.; Peng, C.; Huang, T.; Yao, S.; Tian, Y.; Chang, T.; Zeng, R.; Zou, B. Polaronic Magnetic Excitons and Photoluminescence in Mn^{2+}-Doped $CsCdBr_3$ Metal Halides. *J. Phys. Chem. C* **2021**, *125*, 18031−18039.
(68) Guo, J.; Fu, Y.; Lu, M.; Zhang, X.; Kershaw, S. V.; Zhang, J.; Luo, S.; Li, Y.; Yu, W. W.; Rogach, A. L.; Zhang, L.; Bai, X. Cd-Rich Alloyed $CsPb_{1-x}Cd_xBr_3$ Perovskite Nanorods with Tunable Blue Emission and Fermi Levels Fabricated through Crystal Phase Engineering. *Adv. Sci.* **2020**, *7*, No. 2000930.
(69) Park, N.-G. Perovskite Solar Cells: An Emerging Photovoltaic Technology. *Mater. Today* **2015**, *18*, 65−72.

(70) Lee, J.-H.; Bristowe, N. C.; Lee, J. H.; Lee, S.-H.; Bristowe, P. D.; Cheetham, A. K.; Jang, H. M. Resolving the Physical Origin of Octahedral Tilting in Halide Perovskites. *Chem. Mater.* **2016**, *28*, 4259−4266.
(71) Shahrokhi, S.; Dubajic, M.; Dai, Z.-Z.; Bhattacharyya, S.; Mole, R. A.; Rule, K. C.; Bhadbhade, M.; Tian, R.; Mussakhanuly, N.; Guan, X.; Yin, Y.; Nielsen, M. P.; Hu, L.; Lin, C.-H.; Chang, S. L. Y.; Wang, D.; Kabakova, I. V.; Conibeer, G.; Bremner, S.; Li, X.-G.; Cazorla, C.; Wu, T. Anomalous Structural Evolution and Glassy Lattice in Mixed-Halide Hybrid Perovskites. *Small* **2022**, *18*, No. 2200847.
(72) Zhang, W.-X.; Chen, S.-L.; Shang, Y.; Yu, Z.-H.; Chen, X.-M. Molecular Perovskites as a New Platform for Designing Advanced Multi-Component Energetic Crystals. *Energy Mater. Front.* **2020**, *1*, 123−135.
(73) Li, Y.; Shao, W.; Chen, L.; Wang, J.; Nie, J.; Zhang, H.; Zhang, S.; Gao, R.; Ouyang, X.; Ouyang, X.; Xu, Q. Lead-Halide Cs_4PbBr_6 Single Crystals for High-Sensitivity Radiation Detection. *NPG Asia Mater.* **2021**, *13*, 40.
(74) Dursun, I.; De Bastiani, M.; Turedi, B.; Alamer, B.; Shkurenko, A.; Yin, J.; El-Zohry, A. M.; Gereige, I.; AlSaggaf, A.; Mohammed, O. F.; Eddaoudi, M.; Bakr, O. M. $CsPb_2Br_5$ Single Crystals: Synthesis and Characterization. *ChemSusChem* **2017**, *10*, 3746−3749.
(75) Han, C. C.; Ziya Akcasu, A. Concentration Dependence of Diffusion Coefficient at Various Molecular Weights and Temperatures. *Polymer* **1981**, *22*, 1165−1168.
(76) Yuan, B.; Li, N.; Liu, J.; Xu, F.; Li, C.; Juan, F.; Yu, H.; Li, C.; Cao, B. Improving the Performances of $CsPbBr_3$ Solar Cells Fabricated in Ambient Condition. *J. Mater. Sci. Mater. Electron.* **2020**, *31*, 21154−21167.
(77) Liu, X.; Ren, S.; Li, Z.; Guo, J.; Yi, S.; Yang, Z.; Hao, W.; Li, R.; Zhao, J. Flexible Transparent High-Efficiency Photoelectric Perovskite Resistive Switching Memory. *Adv. Funct. Mater.* **2022**, *32*, No. 2202951.
(78) Tang, Y.; Liang, M.; Zhang, M.; Honarfar, A.; Zou, X.; Abdellah, M.; Pullerits, T.; Zheng, K.; Chi, Q. Photodetector Based on Spontaneously Grown Strongly Coupled $MAPbBr_3$/N-RGO Hybrids Showing Enhanced Performance. *ACS Appl. Mater. Interfaces* **2020**, *12*, 858−867.
(79) Chen, D.; Li, J.; Chen, X.; Chen, J.; Zhong, J. Grinding Synthesis of $APbX_3$ (A = MA, FA, Cs; X = Cl, Br, I) Perovskite Nanocrystals. *ACS Appl. Mater. Interfaces* **2019**, *11*, 10059−10067.
(80) Garza-Hernández, R.; Carrillo-Castillo, A.; Martínez-Landeros, V. H.; Martínez-Puente, M. A.; Martínez-Guerra, E.; Aguirre-Tostado, F. S. In-Situ X-Ray Photoelectron Spectroscopy Analysis of the Initial Growth of CdS Thin Films by Chemical Bath Deposition. *Thin Solid Films* **2019**, *682*, 142−146.
(81) Kirklin, S.; Saal, J. E.; Meredig, B.; Thompson, A.; Doak, J. W.; Aykol, M.; Rühl, S.; Wolverton, C. The Open Quantum Materials Database (OQMD): Assessing the Accuracy of DFT Formation Energies. *npj Comput. Mater.* **2015**, *1*, 15010.
(82) Saal, J. E.; Kirklin, S.; Aykol, M.; Meredig, B.; Wolverton, C. Materials Design and Discovery with High-Throughput Density Functional Theory: The Open Quantum Materials Database (OQMD). *JOM* **2013**, *65* (11), 1501−1509.
(83) Luo, Y.-R. *Comprehensive Handbook of Chemical Bond Energies*; CRC Press: Boca Raton, 2007, DOI: 10.1201/9781420007282.
(84) Lippert, E. *The Strengths of Chemical Bonds*, Cottrell, Von T. L.. Butterworths Publications Ltd.: London, 1958. Aufl, X. 317 S., Geb.t—/32/—. *Angew. Chem.* **1960**, *72*, 602−602.
(85) Powell, C. *X-Ray Photoelectron Spectroscopy Database XPS,Version 4.1, NIST Standard Reference Database 20*, 1989, DOI: 10.18434/T4T88K.
(86) Xu, T.; Xiang, W.; Kubicki, D. J.; Liu, Y.; Tress, W.; Liu, S. Simultaneous Lattice Engineering and Defect Control via Cadmium Incorporation for High-Performance Inorganic Perovskite Solar Cells. *Adv. Sci.* **2022**, *9*, No. 2204486.
(87) *Materials Data on CdBr2 by Materials Project; mp-568690; Lawrence Berkeley National Lab. (LBNL)*, LBNL Materials Project: Berkeley, CA (United States), 2020, DOI: 10.17188/1274644.
(88) Møller, Chr. K.; Saarinen, H.; Näsäkkälä, E.; Pouchard, M.; Hagenmuller, P.; Andresen, A. F. About the Crystal Structure of Cesium Cadmium Tribromide and Some Observations on Crystals of Cesium Cadmium Trichloride. *Acta Chem. Scand.* **1977**, *31a*, 669−672.

https://doi.org/10.1021/acs.chemmater.3c01440
Chem. Mater. 2023, 35, 8909−8921